1 Electronic Supplementary Material of

2 Spatiotemporal and spectroscopic investigations of the secondary plasma generated during double-
3 pulse laser-induced breakdown in bulk water

4 Boyang Xue, Ye Tian, Nan Li, Qingyang Li, Yuan Lu and Ronger Zheng†

5 College of Information Science & Engineering, Ocean University of China, Qingdao 266100, China

6
7 †Corresponding Author: Ronger Zheng, rzheng@ouc.edu.cn

8 1. Temporal evolution of the first laser formed bubble

9 The temporal evolution of the first laser formed bubble (LFB) were obtained by shadowgraphic
10 measurements, as shown in Fig. S1. It can be observed that the LFB expands reaching its maximum
11 volume at 120 μs after the first laser pulse. From then on, the LFB starts to shrink and collapses at
12 240 μs. There also exists twice rebounds of smaller bubbles (250-310 μs, 310-350 μs), which
13 finally disappear after 350 μs.
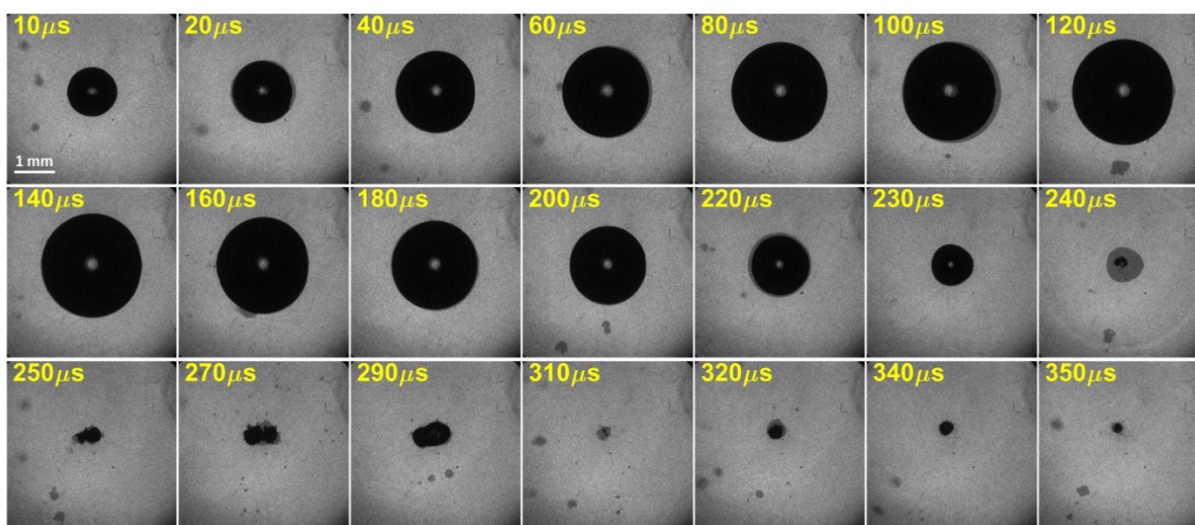
14
15 Figure S1. Time-resolved shadowgraph images of the first laser formed bubble (E_1 = 6mJ). The laser was
16 incident from the right-side. The number on the top-left of each image stands for the delay between the first
17 laser pulse and image measurement. Each shadowgraph is recorded from independent breakdown event, by
18 using the flash lamp for illumination (duration ~ 10 μs) and the ICCD camera for imaging (gate width ~ 1
19 μs).

20 From the time-resolved shadowgraph images presented above, the temporal evolution of bubble
21 radius R can be extracted (cf. black circles in Fig. S2a). The maximum bubble radius determined
22 is 1.3 mm, corresponding to the delay time of 120 μs after the first laser pulse. By fitting R^2 with
23 a fifth order polynomial regression[1], an accurate interpolation of bubble radius R can be obtained
24 (cf. black trace in Fig. S2a). The dynamics of laser-induced bubble can be described by a
25 generalized Rayleigh-Plesset equation[2]:

$$\frac{P_B(t) - P_\infty}{\rho_l} = R(t)\frac{d^2R(t)}{dt^2} + \frac{3}{2}\left[\frac{dR(t)}{dt}\right]^2 + \frac{4\eta_l}{R(t)}\frac{dR(t)}{dt} + \frac{2\sigma_l}{\rho_l R(t)}$$

1 (1),

2 where R is the radius of bubble, $P_B(t)$ is the inner pressure of the bubble, P_∞ is the ambient liquid
3 pressure (10^5 Pa), and ρ_l, η_l, σ_l are the density, dynamic viscosity and surface tension of water,
4 respectively.

5 Assuming an adiabatic van der Waals equation of state for the bubble interior without heat and
6 mass exchange, the vapor pressure and temperature inside the bubble can be given by[2-4]:

$$P_B(t) = \left(P_\infty + \frac{2\sigma_l}{R}\right)\left(\frac{R_\infty^3 - h^3}{R^3 - h^3}\right)^\gamma$$

7 (2),

$$T(t) = T_\infty \left(\frac{R_\infty^3 - h^3}{R^3 - h^3}\right)^{\gamma-1}$$

8 (3),

9 where R_∞ is the radius at which the inner pressure equals to the ambient pressure (0.43 mm used
10 here), T_∞ is the initial temperature (451 K used here), h is the radius determined by the excluded
11 volume of water molecules ($h = R_\infty/9.174$)[2], and $\gamma = C_p/C_v = 1.13$ is the ratio of specific heats.

12 According to the Rayleigh-Plesset model, the temporal evolution of the internal pressure and
13 temperature of the first LFB have been calculated, which are depicted in blue dashed line and
14 magenta solid line in Fig. S2b, respectively. As the first LFB expands reaching the maximum
15 radius at 120 μs, its inner pressure reduces at saturated vapor pressure (P_{min} = 2330 Pa) and the
16 inner temperature approaches to ambient temperature (T_{min} = 293 K)[5-6]. The low pressure at the
17 maximum expansion is considered to be the optimal background condition for underwater DP-
18 LIBS experiments[4]. Hence, the inter-pulse delay corresponding to the maximum expansion of the
19 first LFB, *i.e.* 120 μs, is used in the present work.
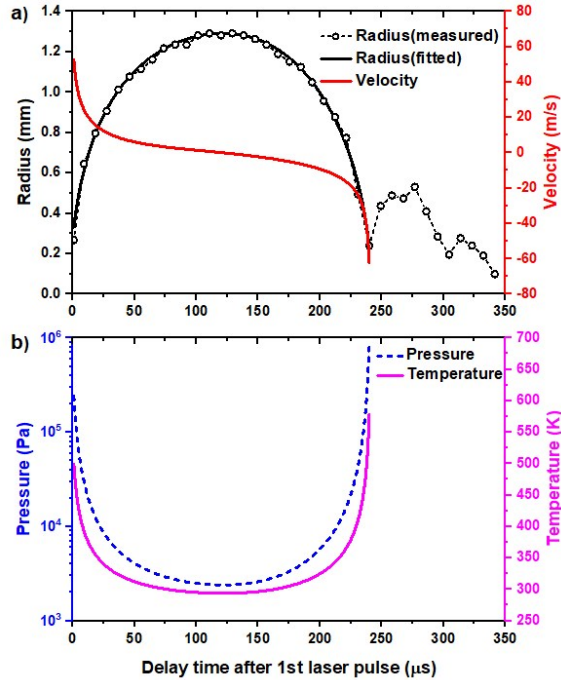
1

2 Figure S2. (a) Temporal evolution of the bubble radius and wall velocity after the first laser pulse. The
3 black circles in (a) are the raw data extracted from bubble images shown in Fig. S1, whereas the black solid
4 line is the corresponding polynomial regression and the red solid line is the wall velocity calculated basing
5 on the fitted curve of bubble radius. (b) Calculated inner pressure (blue dashed line) and temperature
6 (magenta solid line) of the first laser formed bubble as a function of time.

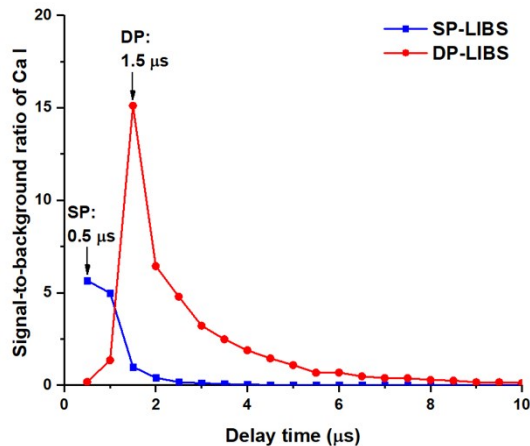7 **2.   Comparison of the typical spectra of SP-LIBS and DP-LIBS in bulk water**

8 For a comprehensive understanding, the typical emission spectrum of underwater DP-LIBS
9 induced by a combination of $E_1 = 6$ mJ and $E_2 = 30$ mJ, is further compared with that of SP-LIBS
10 induced by 6 mJ and 36 mJ, respectively. The spectra were recorded with a gate delay of 300 ns
11 and a gate width of 2000 ns. Although the laser pulse energy increases from 6 mJ to 30 mJ, only
12 the calcium atomic line at 422.7 nm can be observed in the case of SP-LIBS (*cf.* Fig. S3a and Fig.
13 S3b). In contrast, the spectrum of DP-LIBS exhibits more lines with higher ionization and
14 excitation states, *e.g.*, Ca II at 393.4 /396.8 nm and H I at 656.3 nm. Quantitively, the peak intensity
15 of Ca I increased by 3-fold when the laser pulse energy was changed from 6 mJ to 36 mJ in SP-
16 LIBS, while the DP-LIBS resulted in 10-fold increment of Ca I intensity with respect to SP-LIBS
17 at 36 mJ. The energy effect can be excluded when comparing the spectrum of SP-LIBS and DP-
18 LIBS with identical input energy (36 mJ, *cf.* Fig. S3b and Fig. S3c). Thus, we confirm that the
19 excitation efficiency of double-pulse is much higher than that of single-pulse.
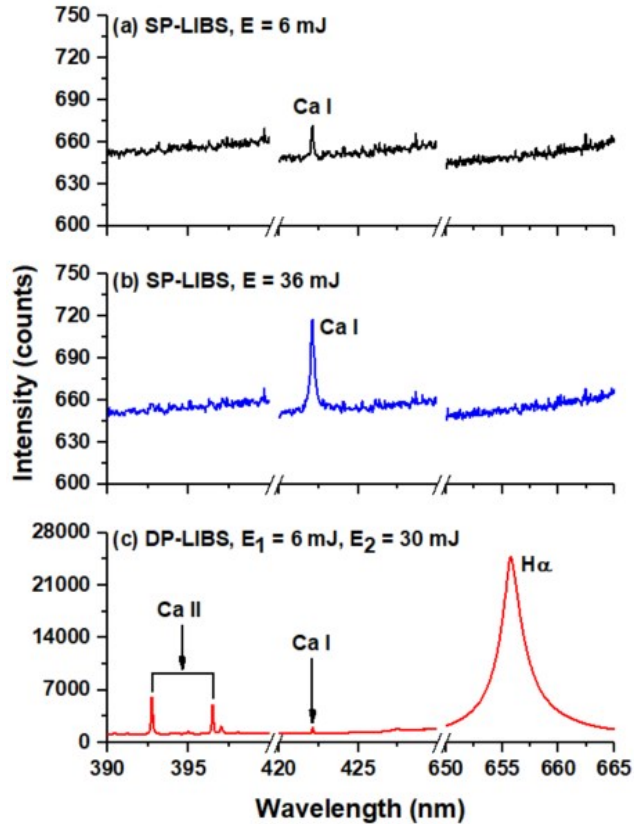
1

2 Figure S3. The typical emission spectra of underwater SP-LIBS induced by the laser pulse energy of 6 mJ
3 (a) and 36 mJ (b), in comparison to that of underwater DP-LIBS induced by the combination of 6 mJ and
4 30 mJ (c). The spectra are recorded with a gate delay of 300 ns and a gate width of 2000 ns.

5 The time-resolved SBR (signal-to-background ratio) of the calcium atomic line at 422.7 nm, was
6 estimated for SP-LIBS and DP-LIBS, respectively (*cf.* Fig. S4). Then the delay time corresponding
7 to the maximum SBR was determined to be 0.5 μs for SP-LIBS and 1.5 μs for DP-LIBS. Further
8 comparison of the spectra between SP-LIBS and DP-LIBS at the maximum SBR delay condition
9 is given in Fig. S5. It can be seen that the spectrum of underwater SP-LIBS is still dominated by
10 the calcium atomic line at 422.7 and the CaOH molecular bands at 554.0/623.0 nm, while the ionic
11 emissions (Ca II 393.4/396.8 nm) are rather weak. In contrast, the spectrum of underwater DP-
12 LIBS possesses more emission lines stemming from higher excitation states. Here, the differences
13 of spectral components between SP-LIBS and DP-LIBS at the maximum SBR delay condition are
14 similar to that obtained at identical delays of 1.5 μs and 3 μs (*cf.* Fig. 2).

Figure S4. The signal-to-background ratio of the calcium atomic line at 422.7 nm as a function of delay time, in the case of SP-LIBS (blue squares and trace) and DP-LIBS (red circles and trace) respectively. The spectra were recorded with a gate width of 500 ns.
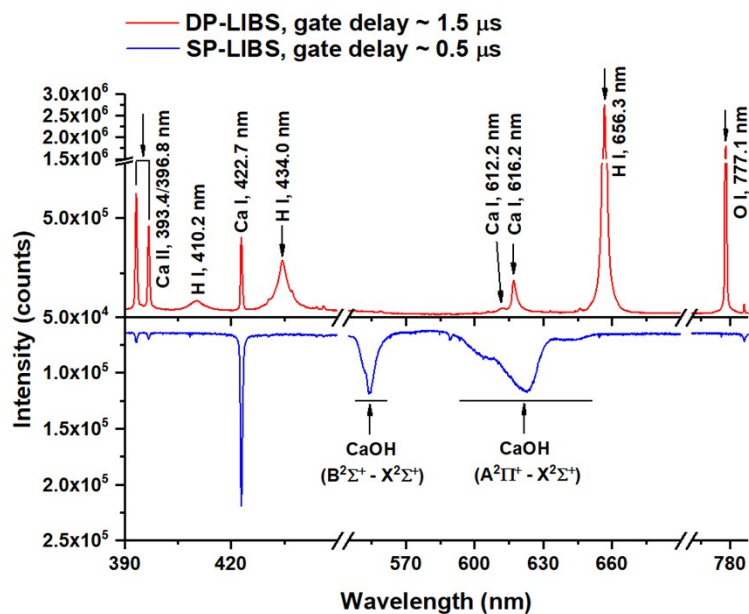
Figure S5. Comparison of the spectra between underwater SP-LIBS (30 mJ, the blue trace in the bottom chart) and DP-LIBS (6 mJ and 30 mJ, the red trace in the top chart) at the maximum SBR delay condition. The spectra are recorded at gate delays of 0.5 μs for SP-LIBS and 1.5 μs for DP-LIBS, with a gate width of 500 ns.

3. Temporally resolved, spatially integrated plasma temperature and electron density

By carefully inspecting the time-resolved spectra of underwater DP-LIBS, it is found that the estimation of plasma parameters (electron density and temperature) is challenging due to the limited number of lines available in the spectrum. When using the 500 ppm Ca^{2+}-containing water solution as the sample, only resonant lines of Ca II 393.4, 396.8 nm and Ca I 422.7 nm are observable throughout a wide span of the plasma lifecycle. However, these resonant lines are quite susceptible to self-absorption, which would severely distort the line profile[7]. Although there are

some non-resonant lines induced by double-pulse, the persistence of each individual cannot cover the entire plasma lifecycle. For instance, the emission of calcium atomic line at 442.5 nm (4.680→1.879 eV) appears at 50 ns but rapidly extinguishes at around 550 ns, while the hydrogen atomic lines occur after a delay of 500 ns, and persist until 2 μs. For electron density determination, H-β line is commonly used as the first choice, because of its high intensity, sufficiently large line broadening, and relatively small possibility of self-absorption[7]. Considering the non-resonant factor and transient features of the spectrum, the calcium atomic line at 442.5 nm and hydrogen atomic line at 486.1 nm (H-β) were combined to estimate the electron density of DP-LIP in the early stage and in later stage respectively. Specifically, the electron density was estimated from the Stark-broadening of Ca I at 442.7 nm and H I at 486.1 nm. If the electron density is higher than 10^{15} cm^{-3}, which is generally valid for a long period of time after plasma formation, the line profiles will be dominated by Stark broadening, while Doppler and natural broadening can be negligible[7]. However, the measured line profiles may be distorted by the instrumental broadening, including the influences of the entrance slit, grating and detector of the spectrometer. The instrumental line shapes are usually close to Gaussian profile[8-9]. Thus, the observable spectral line profile is the convolution of the Stark-broadening (Lorentzian) and the instrumental (Gaussian) contributions, resulting in the Voigt profile. Practically, the experimental spectral lines of Ca I 442.5 nm and H I 486.1 nm were fitted to a good degree of accuracy by the Voigt function ($R^2 > 0.98$).

For deconvolution of the Stark-broadening component, the knowledge of the fixed Gaussian, *i.e.,* the instrumental broadening (Acton SP-2500i, 300 g/mm grating, 50 μm slit width, 13 μm pixel size) is also needed[8-9]. Here a low-pressure Hg lamp (SOFN Instruments Co., Ltd, 7ILM3) was used as the light source for the measurement of the instrumental profile, whose intrinsic linewidth can be neglected comparing to the instrumental linewidth. The FWHM (full width at half maximum) of the inherent lines at 404.66 nm, 435.83 nm and 546.07 nm were determined as 0.508 nm, 0.507 nm and 0.504 nm, respectively. Considering the spectral region of interest, we extrapolated the data, and derived the instrumental linewidth at the wavelength of 442.5 nm and 486.1 nm as 0.507 nm and 0.506 nm, respectively. With such pre-determined Gaussian fraction, the Stark-broadening linewidth was then approximated from the experimentally fitted Voigt FWHM[10]:

$$\Delta\lambda_{FWHM,L} \approx \Delta\lambda_{FWHM,V} - \frac{\Delta\lambda_{FWHM,G}^2}{0.9\Delta\lambda_{FWHM,V} + 0.1\Delta\lambda_{FWHM,G}} \quad (4),$$

where $\Delta\lambda_{FWHM,V}$ is the Voigt FWHM, $\Delta\lambda_{FWHM,G}$ is the Gaussian linewidth, $\Delta\lambda_{FWHM,L}$ is the Lorentzian FWHM. This empirical formula can offer overall high accuracy with no constraints on Gaussian (instrumental broadening) and Lorentzian (Stark-broadening) contributions.

The hydrogen atom exhibits a linear Stark effect, whereas other atoms exhibit a quadratic Stark effect. In the early stage, when using the calcium atomic line at 442.5 nm (non-hydrogen-like), the relation between the electron density and the Lorentzian FWHM of the line can be described as:

$$\Delta\lambda_{FWHM,\ L} \approx 2 \times 10^{-16} w N_e \quad (5),$$

1   which mainly considers the contribution from electron broadening[7]. Here w is the electron impact

2   parameter at $N_e = 10^{16} cm^{-3}$, with an approximate value of 8.14×10^{-2} Å ($T\sim10000$ K) for the line

3   of Ca I 442.5 nm[11].

4   In the later stage, by using the H-β line with linear Stark effect, the relation between the electron

5   density and the Lorentzian FWHM is given by:

6   $N_e = C(N_e, T_e)\Delta\lambda_{FWHM,L}^{3/2}$ (6),

7   where the coefficient $C(N_e, T_e)$ depends weakly on N_e and T_e, with a value of 2.98×10^{14} Å$^{-3/2}$cm^{-3} for

8   the H-β line at $T_e \sim 10000$ K and $N_e \sim 10^{17}$ cm^{-3}.[7, 11]

9   The estimated electron densities from Ca I 442.5 nm and H I 486.1 nm are shown as black squares

10   and red circles respectively, in Fig. S6. Similar values can be found at the conjunction of the two

11   stages around 550 ns. The combined profile suggests transient increasing processes of the electron

12   density at the delay time of 250 ns and 550 ns.
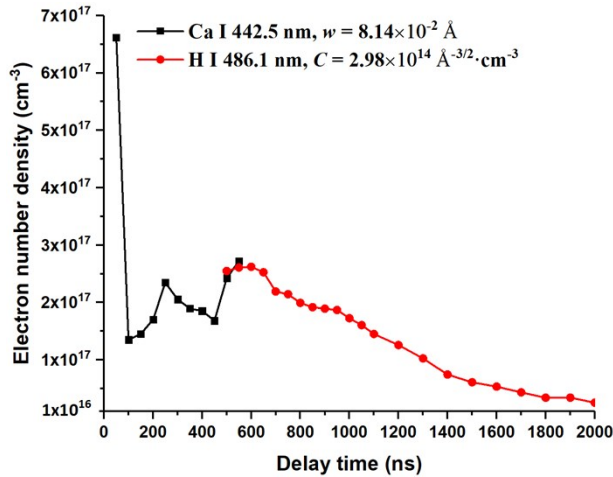
13

14   Figure S6. Electron number density of the secondary plasma induced by double-pulse as a function of time.

15   The black, red markers and traces correspond to the electron number density estimated from the Ca I at

16   442.5 nm and H I at 486.1 nm, respectively. The dataset is recorded with a gate width of 50 ns before the

17   delay time of 1050 ns, and with a gate width of 100 ns for the later delay times.

18   For the estimation of plasma temperature, the Saha-Boltzmann plot method of Ca II 393.4/396.8

19   nm and Ca I 422.7 nm is commonly used for underwater-LIP. Prior to the application of this

20   method, the self-absorption effects of the involved lines have been evaluated with a qualitative

21   indicator, *i.e.*, the intensity ratio of the two resonant Ca II lines at 393.4 nm and 396.8 nm. As the

22   two Ca II lines correspond to the same ground state, the self-absorption would affect the stronger

23   one (393.4 nm) more severely. Therefore, a large value of the intensity ratio, I_{393nm}/I_{396nm}, would

24   indicate a weak self-absorption effect, while a small value would indicate a heavy self-

25   absorption[12]. In the present experimental condition, it was found that only in the later stage (after

26   ~500 ns), this intensity ratio could maintain a relatively high and stable value (*cf.* red circles and

27   trace in Fig. S7), ensuring a mild effect of self-absorption on the temperature evaluation.

28   Accordingly, after the delay of 500 ns, the intensities of Ca II 393.4/396.8 nm and Ca I 422.7 nm

29   as well as the electron density in Fig. S6 were employed to determine the plasma temperature

1 through the Saha-Boltzmann plot. As shown in Fig. S7, the temperature of the underwater DP-LIP
2 presents a slow decay and remains higher than 6000 K within the delay of 2 µs.
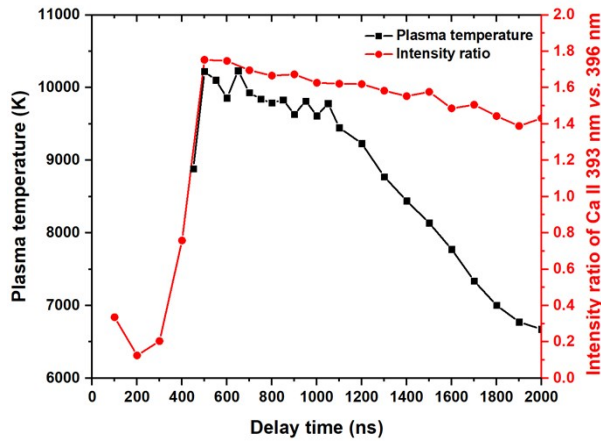
3

4 Figure S7. The plasma temperature (black squares and black trace) of underwater DP-LIP and the
5 corresponding intensity ratio of the two resonant Ca II lines (I_{393nm}/I_{396nm}, red circles and red trace) as a
6 function of delay time. The left and right axes are assigned with the same color as the markers/traces. The
7 dataset is recorded with a gate width of 50 ns before the delay time of 1050 ns, and with a gate width of
8 100 ns for the later delay times.

9 **4. Composite images of different species**
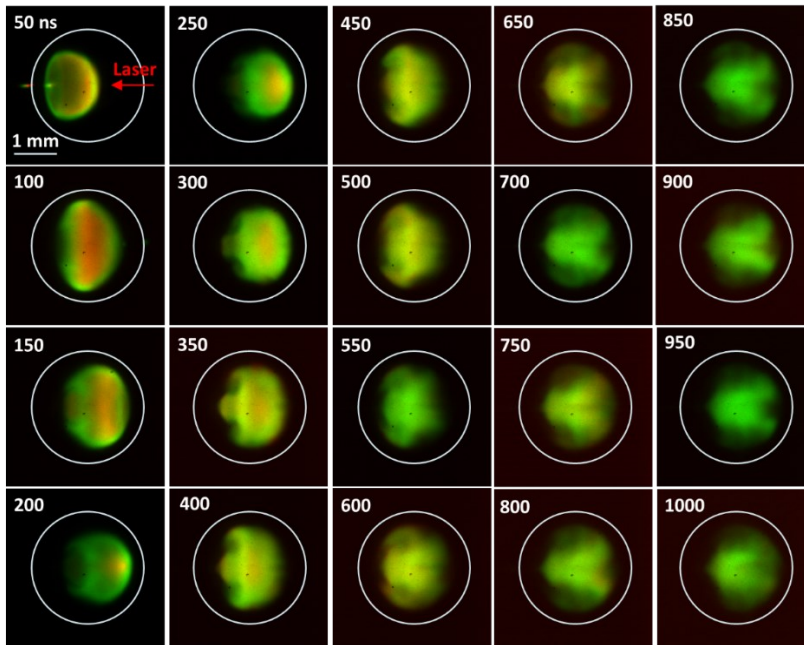
10

11 Figure S8. Composite images of the species-specific emissions from Ca I and H I at different delay times.
12 The red color scale is used for representing the emission intensity of the Ca I emitter, while the green color
13 scale is set for the emitter of H I. The laser beams are incident from the right-side, and the white cycle in
14 each image corresponds to the boundary of the first LFB.

15 **5. Temporal evolution of the second laser formed bubble without and with the first laser pulse**

1 The time-resolved shadowgraph images of the second laser formed bubble were obtained with
2 laser 1 on (*cf.* main text, Fig. 8) and laser 1 off (data not shown). Then the corresponding temporal
3 evolution of the bubble radius can be extracted from the shadowgraph images (*cf.* black circles in
4 Fig. S9). According to the Rayleigh-Plesset model (*cf.* SI, Section 1), the temporal evolution of
5 the inner pressure of the second LFB have been calculated, which are depicted in blue dotted line
6 (*cf.* Fig. S9).

7 As shown in Fig. S9, with laser 1 on, *i.e.,* the maximum radius of the second LFB was 0.92 mm at
8 the delay time of 120 μs. In contrast, with laser 1 off, the second LFB can expand to reach a much
9 larger maximum radius, 3.34 mm, at the delay of 200 μs. It indicates that, with the existence of the
10 first LFB, only a small amount of the second laser pulse energy ($E_2 = 30$ mJ) can be deposited into
11 the second LFB. Notably, with laser 1 on, during the lifecycle of the downstream part of the
12 secondary plasma (≤ 6 μs), the second LFB is confined in a small volume ($R < 0.4$ mm), and
13 corresponds to a relatively high inner pressure ($P_B \sim 0.5 \times 10^5$-7.6×10^5 Pa).

14
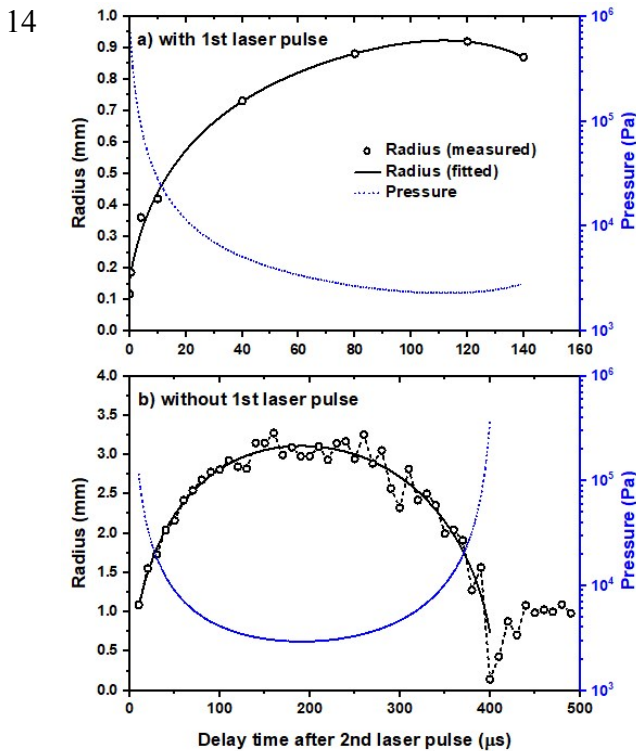
16 Figure S9. Temporal evolution of the radius (black circles and solid line) and inner pressure (blue dotted
17 line) of the second laser formed bubble, with laser 1 on (a) and laser 1 is off (b). The black circles represent
18 the raw data extracted from bubble images, which were taken after the second laser pulse with laser 1 on
19 or laser 1 off, and the black solid line is the corresponding polynomial regression.

20

21 **Supplementary References**

22 1. Lam, J.; Lombard, J.; Dujardin, C.; Ledoux, G.; Merabia, S.; Amans, D., Dynamical study of
23   bubble expansion following laser ablation in liquids. *Applied Physics Letters* **2016,** *108* (7), 5.

1 2. Tamura, A.; Sakka, T.; Fukami, K.; Ogata, Y. H., Dynamics of cavitation bubbles generated by
2   multi-pulse laser irradiation of a solid target in water. *Applied Physics a-Materials Science &*
3   *Processing* **2013,** *112* (1), 209-213.
4 3. Brenner, M. P.; Hilgenfeldt, S.; Lohse, D., Single-bubble sonoluminescence. *Reviews of Modern*
5   *Physics* **2002,** *74* (2), 425-484.
6 4. De Giacomo, A.; Dell'Aglio, M.; De Pascale, O.; Capitelli, M., From single pulse to double
7   pulse ns-laser induced breakdown spectroscopy under water: elemental analysis of aqueous
8   solutions and submerged solid samples. *Spectrochimica Acta Part B: Atomic Spectroscopy*
9   **2007,** *62* (8), 721-738.
10 5. Lazic, V.; Jovicevic, S.; Carpanese, M., Laser induced bubbles inside liquids: Transient optical
11   properties and effects on a beam propagation. *Applied Physics Letters* **2012,** *101* (5), 054101.
12 6. Akhatov, I.; Lindau, O.; Topolnikov, A.; Mettin, R.; Vakhitova, N.; Lauterborn, W., Collapse
13   and rebound of a laser-induced cavitation bubble. *Phys. Fluids* **2001,** *13* (10), 2805-2819.
14 7. Singh, J. P.; Thakur, S. N., *Laser-induced breakdown spectroscopy*. Elsevier: 2007.
15 8. Konjevic, N., Plasma broadening and shifting of non-hydrogenic spectral lines; Present status
16   and applications. *Physics Reports-Review Section of Physics Letters* **1999,** *316* (6), 339-401.
17 9. Konjevic, N.; Ivkovic, M.; Sakan, N., Hydrogen Balmer lines for low electron number density
18   plasma diagnostics. *Spectroc. Acta Pt. B-Atom. Spectr.* **2012,** *76*, 16-26.
19 10. Vaczi, T., A New, Simple Approximation for the Deconvolution of Instrumental Broadening
20   in Spectroscopic Band Profiles. *Applied Spectroscopy* **2014,** *68* (11), 1274-1278.
21 11. Griem, H. R., *Plasma Spectroscopy*. McGraw Hill, New York: 1964.
22 12. Tian, Y.; Sokolova, E. B.; Zheng, R. G.; Ma, Q. L.; Chen, Y. P.; Yu, J., Characteristics of the
23   ablation plume induced on glasses for analysis purposes with laser-induced breakdown
24   spectroscopy. *Spectroc. Acta Pt. B-Atom. Spectr.* **2015,** *114*, 7-14.

25